Single-mode porous silicon waveguide interferometers with unity confinement factors for ultra-sensitive surface adlayer sensing

TAHMID H. TALUKDAR,[1] GABRIEL D. ALLEN,[2] IVAN KRAVCHENKO,[3] AND JUDSON D. RYCKMAN[1,*]

[1]*Holcombe Department of Electrical and Computer Engineering, Clemson University, Clemson, South Carolina, 29634, USA*
[2]*Clemson Summer Undergraduate Research Experience Program: Solid State Devices for Electronics, Photonics, and Magnetics Technology, Clemson University, Clemson, South Carolina, 29634, USA*
[3]*Center for Nanophase Materials Science, Oak Ridge National Laboratory, Oak Ridge, TN, 37831, USA*
**jryckma@clemson.edu*

Abstract: Guided wave-optics has emerged as a promising platform for label free biosensing. However, device sensitivity toward surface-bound small molecules is directly limited by the evanescent interaction and low confinement factor with the active sensing region. Here, we report a mesoporous silicon waveguide design and inverse fabrication technique that resolves the evanescent field interaction limitation while achieving maximal transverse confinement factors and preserving single-mode operation. The waveguide sensors are characterized in a Fabry-Perot interferometer configuration and ultra-high sensitivity to small molecule adlayers is demonstrated. We also identify dispersion to be a promising degree of freedom for exceeding the sensitivity limits predicted by conventional non-dispersive effective medium theory.

1. Introduction

Optics has emerged as a powerful tool for biosensing applications. In particular, guided-wave optics has supported a variety of breakthrough technologies which enable the sensitive detection of surface-bound small molecules and other nanoscopic analytes, such as surface plasmon resonance (SPR) [1], guided mode resonance (GMR) [2], nanophotonic waveguides and resonators [3–5], 2D atomic materials [6], and whispering gallery resonators [7], to name only a few. The majority of these sensors can broadly be categorized into two general types of sensing schemes: (1) spectrally sensitive (e.g. Raman scattering or absorption), and (2) phase sensitive (e.g. resonator, interferometer). Phase sensitive devices are especially attractive for their ability to detect almost any molecule or analyte provided that it can be specifically bound or immobilized to a surface through selective surface chemistry, thus not limiting their scope to analytes with well characterized Raman scattering or absorption peaks.

Similar to bulk refractive index sensors (e.g. for bulk liquids) [8], phase sensitive surface adlayer biosensors respond to local changes in refractive index arising from the introduction of the analyte species. While bulk refractive index sensors have been extensively studied and are comparatively straightforward to design by maximizing the confinement factor in the bulk (e.g. liquid) sensing medium [3,8–10], surface adlayer sensors are comparatively more difficult to design as they require maximizing the mode overlap with the surface area of the sensor [11].

Our sensors are composed of uniquely designed and fabricated porous silicon (pSi) waveguides. pSi is attractive owing to its ultra-high surface area (>100 m^2 cm^{-3}), rapid and facile synthesis, and widely tunable porosity and pore dimensions. Previous demonstrations of pSi waveguides have successfully demonstrated enhanced device sensitivities (e.g. compared

to SOI waveguides) owing to the enhanced overlap between the surface adlayer and the optical mode provided by the high surface area [12–14]. However, modern pSi waveguides face limitations with respect to performance and fabrication complexity. First, optimizing sensitivity requires increasing the guided mode's transverse confinement factor within the active sensing region as high as possible, ideally to unity. For 3D pSi strip waveguides, with 2D cross-section, confinement factors >50% are readily achievable [14,15]; however, extending this confinement factor to unity is fundamentally limited by the non-zero evanescent field of a standard strip waveguide and the transition from single-mode to multi-mode that arises with increasing waveguide size [13]. Further, the sensitivity of devices with sub-unity confinement factors is inherently sensitive to fabrication variations which modulate modal confinement. To compete with a robust and scalable biosensing technology, such as SPR, it is desirable to achieve a high sensitivity which is also highly repeatable and extremely tolerant to critical dimension variations introduced during fabrication. Lastly, the wafer-scale fabrication of pSi waveguides typically requires high resolution lithography and etching to be performed on pre-synthesized porous silicon substrates. Such patterning requires delicate process optimization, as resists and process chemicals are prone to infiltrate the porous network, elevating the risk of pore clogging, corrosion, and/or contamination. This motivates the development of alternative fabrication and patterning techniques which can harness the leading benefits of porous silicon's facile and self-organizing synthesis while minimizing fabrication costs and complexity [16–18].

In this work we address the above challenges through the introduction of: (1) a novel inverse processing technique which enables lithography to be performed on standard silicon substrates prior to porosification, and (2) unique single-mode multi-layer rib waveguide designs which enable unity confinement factors to be realized while maintaining single mode operation.

2. Approach

2.1 Theoretical Framework

To address the challenge of maximizing device sensitivity for phase sensitive optical structures (e.g. waveguides, interferometers, resonators), we first review the mathematical definition of sensitivity. The sensitivity of a waveguide's effective index, n_{eff}, to changes in the refractive index of an active sensing region, with index n_A, can be expressed as:

$$S_1 \equiv \frac{\partial n_{eff}}{\partial n_A} \tag{1}$$

This sensitivity may be derived via first-order perturbation theory, under the general case of potentially high index contrast waveguides under the assumption of low material dispersion [19], as:

$$S_1 = \frac{n_g}{n_A}\frac{\iint_A \varepsilon|E|^2 dxdy}{\iint_\infty \varepsilon|E|^2 dxdy} = \frac{n_g}{n_A}\Gamma_A \tag{2}$$

Where n_g is the group index of the guided wave and Γ_A is the transverse confinement factor which describes the fraction of electric field energy confined in the active sensing region of the device. Per Eq. (2), maximizing the sensitivity generally requires: (1) a device with a high group index, and (2) a device which maximizes the transverse confinement factor Γ_A and therefore the common region between the optical mode and the device's active sensing area. Note: achieving high values of n_g/n_A equates to achieving a high electric field energy density along the optical propagation axis, which can readily be achieved via slow light waveguide designs (at the cost

of also enhancing propagation losses by the same factor) [20], whereas the maximization of Γ_A is an as of yet unresolved topic, especially in the context of surface adlayer sensors, and is a particular focus of this work. We also note that the wavelength sensitivity of a waveguide based optical resonator, with units [nm/RIU], can be expressed as $\Delta\lambda/\Delta n_A = \lambda_0/n_g S_1$ [21].

The generalized index sensitivity, S_1, can be redefined for our application of the detection of small molecular adlayers which bind to the surface of the sensor within the active sensing region. Here, surface sensitivity, S_2, is redefined as the waveguide effective index change per change in adlayer thickness [units: RIU /nm] or alternatively in terms of waveguide effective index change per change in adlayer mass surface density [units: RIU $pg^{-1}\,mm^2$] as:

$$S_2 \equiv \frac{\partial n_{eff}}{\partial \sigma} = \frac{\partial n_{eff}}{\partial n_A}\frac{\partial n_A}{\partial \sigma} = S_1 \frac{\partial n_A}{\partial \sigma} \tag{3}$$

For bulk index sensing, maximizing sensitivity S_1 has a relatively straightforward requirement of driving Γ_A toward unity by maximizing mode confinement in the cladding regions which are accessible to the bulk sensing medium (e.g. liquid) [8]. This task can be achieved by tailoring the mode confinement and/or evanescent nature of the optical wave, as demonstrated in surface plasmon-polariton based devices [22], hollow core devices [9], and guided mode resonance structures on ultra-low index substrates [23]. For surface sensing however, a trade off quickly arises in that increasing the electric field intensity at the surface simultaneously increases the evanescent field strength and the transverse confinement factor with the cladding region. Optimal confinement factors in the active sensing region (at the waveguide surface) are generally found by balancing this trade-off [3]. For a molecular adlayer thickness of 1 nm the transverse confinement factor Γ_A is typically on the order of ~1% for conventional strip waveguides. The SOI waveguide confinement factor can be increased to the range of approximately ~2-5% for optimized TM strip waveguide modes and TE slot waveguide modes respectively [3,24]. Such SOI designs produce a benchmark surface adlayer sensitivity $S_2 \approx 5 \times 10^{-4}$ [RIU/nm]. In this article, we report waveguide designs that reach sensitivity values $S_2 > 7\times 10^{-2}$ [RIU/nm], more than two orders of magnitude higher than the SOI benchmark. Further, in our investigation of waveguide interferometers operating in the unity confinement factor regime, we identify dispersion as a promising new degree of freedom for achieving future sensitivity enhancements.

2.2 Waveguide Design and Inverse Processing Technique

Our inverse processing technique is illustrated in Fig. 1. Silicon wafers are first patterned and etched through electron beam or photo-lithography followed by reactive ion etching (RIE). This patterning step defines the outer dimensions of our rib waveguides. Anodization is then performed in 15% ethanoic hydrofluoric acid solution. This step can optionally be performed at the wafer-scale or after dicing the pre-patterned silicon substrate into smaller dies. During anodization, the applied current density and duration are precisely controlled to create multiple layers of pSi with controlled average pore dimensions, refractive indices, and layer thicknesses. We note that a similar inverse technique has also been utilized to construct novel micro-optical devices from pSi [25].

In this study, we investigate both three-layer (3-L) and two-layer (2-L) pSi waveguide designs which utilize a high index, n ≈ 2.1, pSi core layer cladded by a low index, n ≈ 1.56, pSi layer. In the 3-L design an additional top-cladding pSi layer is etched which harvests all the residual evanescent field and achieves unity confinement factors at smaller core dimensions.

Fig. 2 shows cross-sectional scanning electron microscopy (SEM) images of 3-L waveguide structures fabricated across a waveguide width skew. These images highlight the

unique rib-type geometry that is achieved from our inverse processing technique. As visible here, anodization proceeds preferentially in the <100> family of directions (e.g. normal to the (100) planes on the top surfaces and waveguide sidewalls). To achieve a single-mode rib waveguide design, our waveguide geometry and layer thicknesses are selected such that the opposing etch fronts, which define the core layer (originating from the sidewalls), begin to intersect with each other beneath the rib (i.e. Fig. 2(c)-2(e)). Additional details regarding our processing parameters can be found in Appendix A.

Fig. 3 reveals the simulated confinement factors and surface adlayer sensitivities of our 2-L and 3-L waveguide geometries alongside a comparison to the conventional strip waveguide geometry. We observe consistent, approximately unity, transverse confinement factors for both 2-L and 3-L waveguides. The 2-L waveguide exhibits higher fractional confinement in the pSi

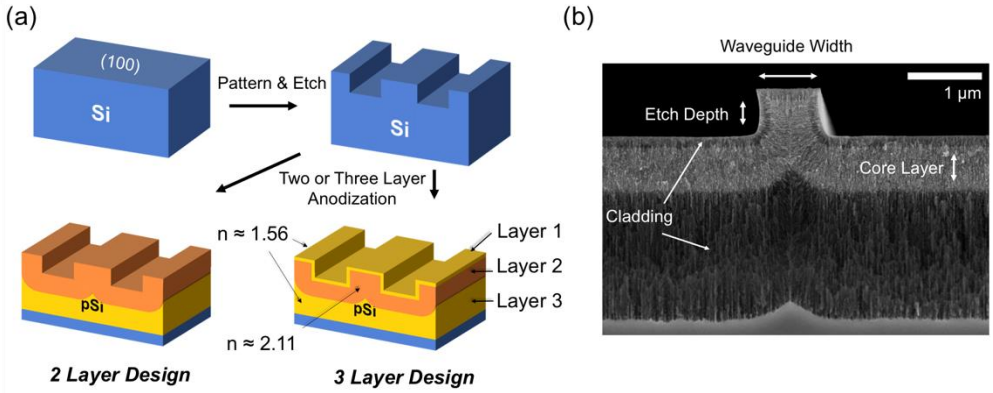

Fig. 2. (a) Inverse fabrication procedure showing patterning of Si wafers followed by anodization to create 2-L or 3-L designs. (b) Spatial design parameters for proposed waveguides showing cross section schematic and SEM image.

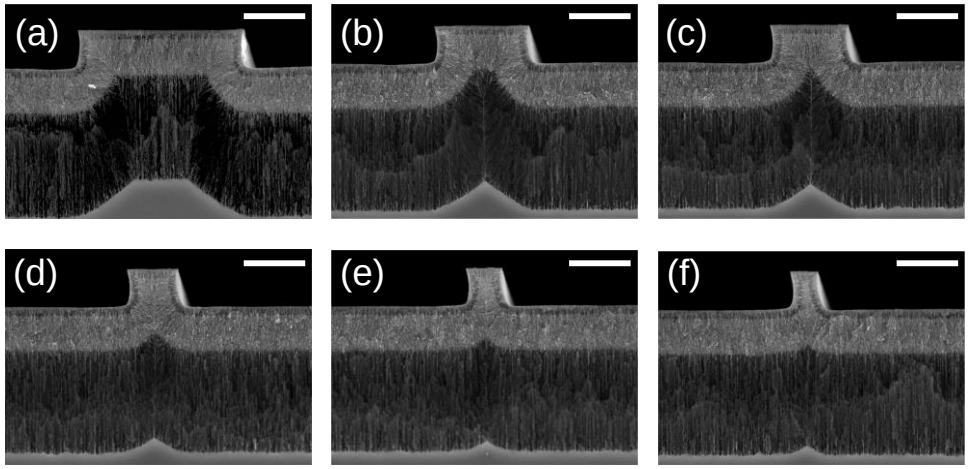

Fig. 1. Cross-sectional SEM of 3-L devices showing variable widths after completing the inverse processing technique (scale bar = 1μm).

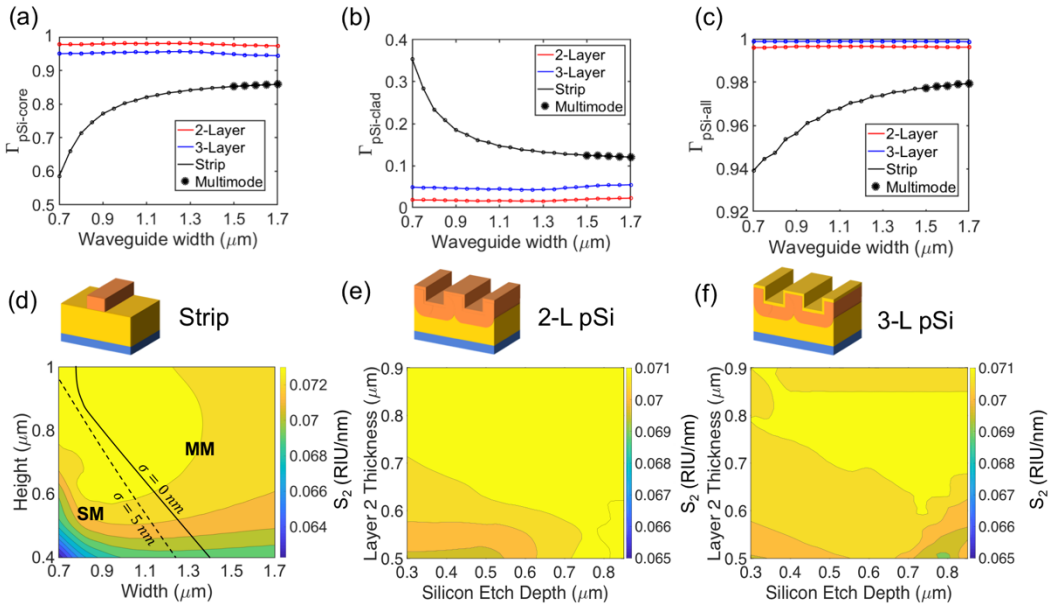

Fig. 3. (a) Confinement factor in the core region (high index pSi) vs. waveguide width for our 2-L and 3-L waveguides and a comparison to conventional strip waveguides. (b) Confinement factor in the cladding region (low index pSi region) vs. waveguide width for 2-layer, 3-L and strip waveguide cladding. (c) Total confinement factor (pSi) vs. waveguide width. (d) strip, (e) 2-layer and (f) 3-L design sensitivity contours (width = 1μm) as a function of waveguide dimensions. For the 3-L design the top cladding is 180 nm and the bottom cladding is 3μm. Single and multimode regimes are defined by the boundary in (d).

core layer while the 3-L waveguide harvests all the residual evanescent field for sensing and confines ~5% of the electric field energy in the ~180 nm top thin cladding layer. Unlike the strip waveguide, both the 2-L and 3-L waveguides retain their single mode characteristics throughout all the dimensions spanned in Fig. 3. The 2-L and 3-L designs further exhibit highly uniform sensitivities which are thus extremely tolerant to fabrication variations. Our calculations show that the strip waveguide geometry can be pushed into an ultra-high confinement factor regime (>90%), when also accounting for the field retained in the pSi cladding (~15%), however as expected they become multimode as confinement approaches unity. Compared to the 2-L and 3-L designs, strip waveguides also show lower confinement in the core region. Moreover, since the core index is significantly perturbed during the act of sensing, the single mode (SM) to multi-mode (MM) cut-off is also highly sensitive to the surface bound adlayer thickness. The SM-MM boundary is highlighted in Fig. 3d for two example cases of adlayer thickness, 0 nm and 5 nm, as calculated at a single wavelength (1600 nm). In a practical implementation of a strip waveguide sensor, it would be necessary to operate away from the optimal sensitivity point to ensure single mode operation across reasonable fabrication variations, sensing corner-cases, and wavelengths of interrogation. The 2-L and 3-L designs meanwhile, guarantee SM operation as well as maximum and consistent sensitivity across a broad fabrication window and optical bandwidth (>100 nm).

3. Results and discussion

3.1 Unity Confinement Factor pSi Waveguide Interferometers

We fabricate 2-L and 3-L waveguides with specific widths that satisfy the geometry where the opposing etch fronts intersect below the core (Fig. 2(d)-2(f)). Fabrication details are described in the experimental section. Chosen waveguide dimensions are utilized to simulate our

waveguide model. Simulations confirm near unity transverse confinement factors of 99.89% and 99.76% for TE and TM modes respectively in the 3-L waveguide, and 99.66% and 99.49% for TE and TM respectively in the 2-L waveguide (Fig. 4). We capture the TE/TM mode shapes on infrared camera and observe them to be consistent with the simulation (Fig. 4(e), 4(f)). We also perturb the position of input coupling fiber and are unable to excite or observe any higher order modes, thus confirming the single-mode nature of these waveguides.

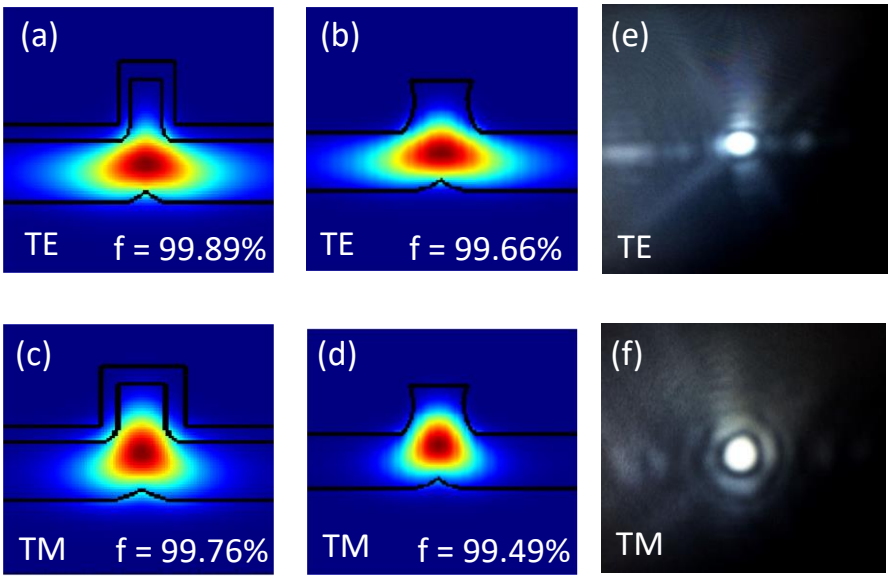

Fig. 4. Simulation of the 900nm 2-layer waveguide reproduced from SEM measurements showing simulated (a) TE and (c) TM mode shape and confinement factor for 3-L waveguides, (b) TE and (d) TM mode shape and confinement factor for 3-L waveguides and (e) TE and (f) TM mode shape captured on IR camera on the 900nm 2-layer waveguide.

Fig. 5 illustrates the experimental measurement setup. Transmission measurements are performed with the waveguides in a Fabry-Perot configuration with waveguide length L between the input and the output cleaved facets with reflectivities R_1 and R_2 respectively. Example transmission data for a 2-layer waveguide is shown in Fig. 5(b). Performing a fast Fourier transform (FFT) on spectra in the frequency domain shows a peak which corresponds to the value $2n_gL$ where n_g is the group index of the guided mode and L is the length of the cavity. Fig. 5(c) shows the value of the group index (n_g) plotted on the same scale for TE and TM modes. For all performed measurements, the TE mode showed a higher group index compared to the TM mode, approximately by 0.15 RIU. This experimentally measured TE/TM index difference is attributed to the anisotropic refractive index of porous silicon, as our simplified waveguide simulation, which approximates the layers with an isotropic refractive index, predicts a difference <0.03 RIU from mode dispersion. We note that the index contrast $\Delta n \approx 0.15$ is comparable to the birefringence noted in other works using porous silicon thin films at ~55% porosity [26,27].

In addition to extracting the waveguide's group index, our measurements allow us to approximate the propagation loss from the spectrum's fringe contrast while assuming facet reflectivities ($R_1 = R_2 \approx 0.11$), which are given by the ideal Fresnel reflection coefficients. We measure the loss from the captured Fabry-Perot fringes (Fig. 5(b)) where the upper bound of the loss is 2.7±0.3 dB/mm. Note: if a given device's facet reflectivities are less than the ideal Fresnel values, i.e. due to an imperfect cleave angle, the measured fringe contrast will be

reduced under the same nominal loss leading to overestimation of the waveguide loss. These losses originate from free carrier absorption in the highly doped p-type silicon skeleton and Raleigh scattering from surface roughness and disorder in the bulk pSi structure.

To characterize waveguide sensitivity to surface adlayers, we perform a proof-of-concept demonstration using 3-aminopropyltriethoxysilane (3-APTES), which is a silane molecule commonly utilized for enhancing surface adhesion between silica and organic molecules [28]. Here, the 3-APTES serves as a ~0.8 nm thick model adlayer, with a refractive index near ~1.46 [29]. Prior to 3-APTES exposure, waveguides are oxidized for 5 minutes at 500°C. The oxidization process lowers the effective index of pSi layers owing to the consumption of high index silicon, resulting in a reduction in effective and group indices; whereas the silane attachment increases the effective index of pSi layers and increases the waveguide effective and group indices. After oxidation we expose the waveguides to 4% 3-APTES, diluted in a H_2O: methanol (1:1) mixture for approximately 45 minutes, followed by

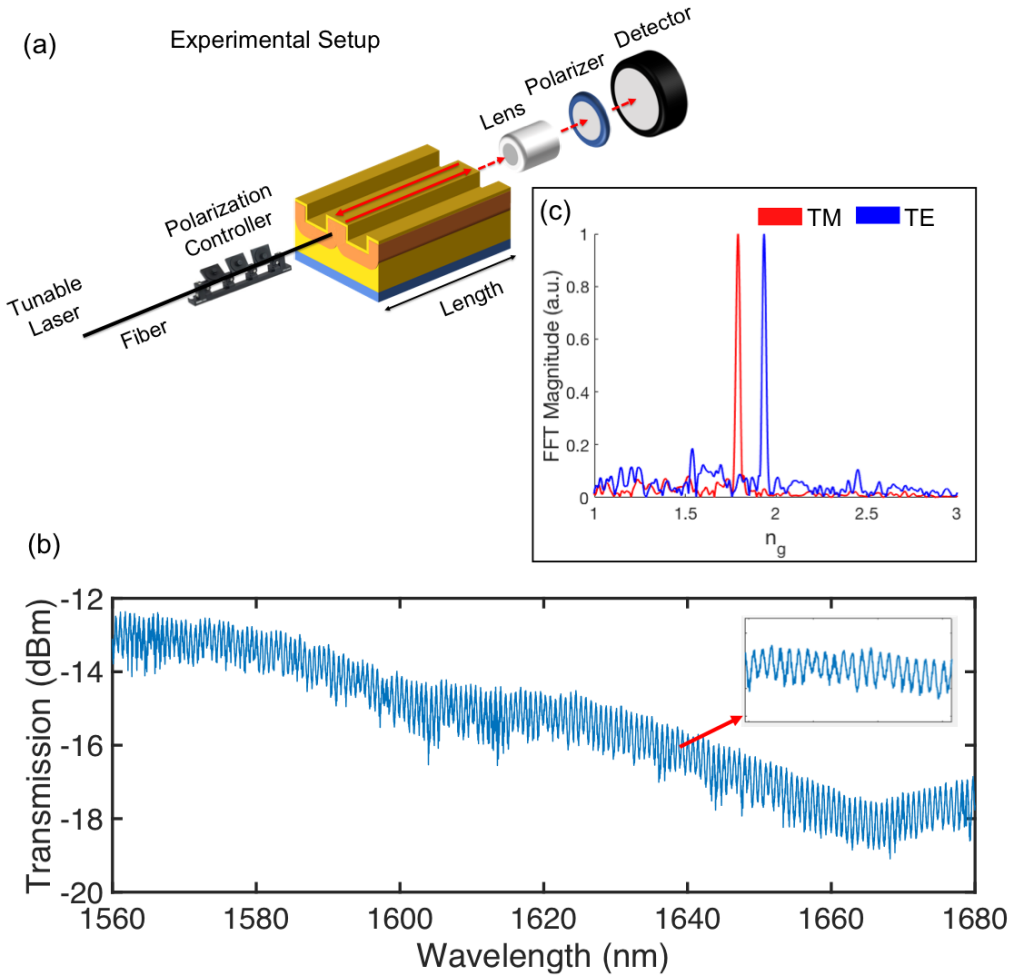

Fig. 5. (a) Experimental setup of the Fabry-Perot configuration for testing the waveguides (b) Spectrum captured from the 1560-1680 nm wavelength sweep (c) FFT analysis reveals peaks corresponding to the waveguide group inex. TE and TM modes are identified using a polarizer.

thorough rinsing in water and drying under air flow. Waveguide transmission spectra are

recorded before and after each step, and the group index is measured via the fast Fourier transform (FFT) method. This approach is similar to pSi thin film biosensors where taking the FFT of an optical spectrum produces a single peak which corresponds to the double pass optical path length ($2n_gL$) of the Fabry-Perot cavity [30,31]. This approach attractively enables sensing to be performed without tracking a specific spectral feature or resonance shift. We also note that owing to the significantly enhanced ~mm scale path length of our devices, i.e. versus the ~µm path length of pSi thin film devices, the interferometric resolution and limit of detection is correspondingly enhanced. This principle is experimentally supported by the ultra-narrow FFT peaks we are able resolve in the Fourier domain, 2-3 orders of magnitude narrower than conventional FFT peaks observed in thin-film pSi biosensors [31].

3.2 Surface Sensing Characterization

Experimental results for wide and narrow 2-L waveguides (900 nm and 500 nm width at the base respectively) are presented in Fig. 6. Transmission spectra was collected under TE polarization and the sensor response is determined as the observed shift in group index Δn_g. Per expectation, the wider waveguide shown in Fig. 6(a) shows a higher nominal group index. After oxidation and silanization, we observe a clear shift in group index between each measurement. As summarized in Table 1, the index reduction due to oxidation in the 2-layer waveguides is approximately $\Delta n_g \approx 0.105$ and the observed index increase due to 3-APTES attachment is approximately $\Delta n_g \approx 0.058$. Considering the ~0.8 nm nominal 3-APTES adlayer thickness [29], the response to silane attachment corresponds to a measured small molecule surface adlayer sensitivity of $\partial n/\partial \sigma \approx$ 0.0725 RIU/nm. This result is in good agreement with the predicted effective index sensitivity S_2 (~0.07 RIU/nm, Fig. 3(d)). We also observe a consistent response Δn_g for both the narrow and wide waveguides which affirms the repeatability of the sensing process and confirms our expectation (Fig. 3) that the sensitivity in our devices is not a strong function of waveguide dimensions.

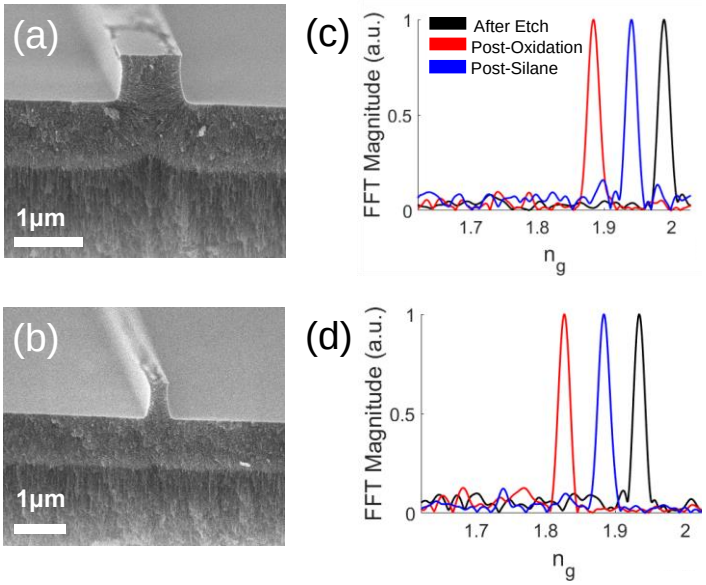

Fig. 6. (a) Cross-section SEM of a 2-layer prototype pSi rib waveguide of 900 nm width. (b) Cross-section SEM of a 2-layer pSi rib waveguide of 500 nm width (c) Group index from the FFT of the spectrum for TE mode for the 900 nm waveguide and (d) for the 500 nm waveguide.

We further experiment with the 3-L designs which have an additional low index high porosity layer of ~180 nm thickness. Fig. 7 shows the 3-L waveguides and measured results for the same experiment detailed above. The blue shift due to oxidation is ~130% larger than the 2-L waveguides, with a measured index reduction $\Delta n_g \approx 0.25$. Here the larger response to oxidation is attributable in part to the increased confinement in the low porosity pSi cladding layers, ~5% in the 3-L waveguide vs. ~2% in the 2-L waveguide. From an effective medium standpoint, higher porosity pSi layers are more sensitive to nanoscale consumption of the Si skeleton. Notably however, the 3-L waveguide also shows an unexpectedly enhanced response to small molecule attachment. The measured group index increases by $\Delta n_g \approx 0.078$ in response to silanization which corresponds to a measured index sensitivity $\partial n/\partial \sigma \approx 0.0975$ RIU/nm, which is ~40% larger than both the 2-L waveguide and the predicted bulk pSi effective index sensitivity S_2 (0.07 RIU/nm). We also observe this enhanced sensitivity to be consistent for different waveguide widths. Remarkably, this sensitivity exceeds the effective medium sensitivity of the bulk porous silicon core medium, which is modelled to be ~0.074 RIU/nm for a 15 nm average pore diameter and ~55% bulk porosity [29].

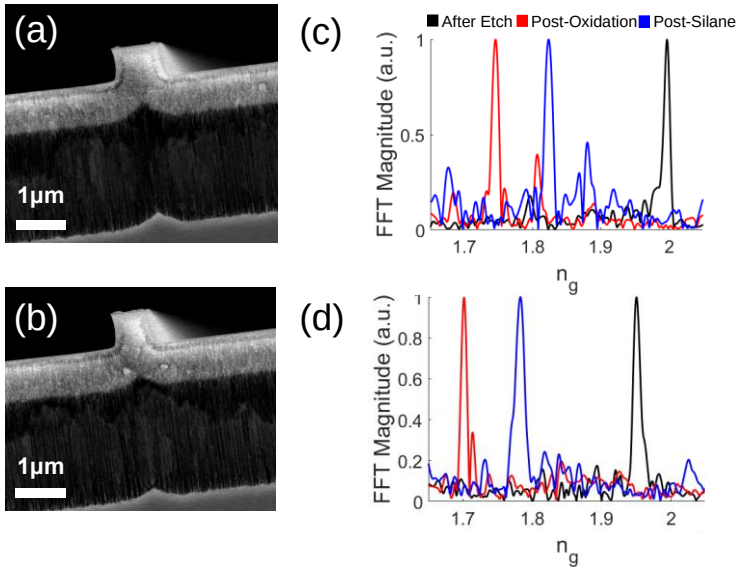

Fig. 7. (a) Cross-section SEM of a 3-L pSi rib waveguide of 700 nm width and (b) 600 nm width. (c) Group index measured from FFT of the spectra for 700 nm waveguide and (d) 600 nm waveguide.

3.3 Exceeding the Sensitivity of Bulk pSi: The Dispersion Degree of Freedom

Here, we posit that the dominant effect producing the observed group index sensitivity enhancement is what we refer to as 'sensitivity dispersion'. Our predicted waveguide sensitivity (Fig. 3) is modelled as a perturbation in the waveguide effective index $\partial n_{eff}/\partial \sigma$ (Eq. 3). Unlike the measurement of a spectral resonance shift, our interferometer measurement extracts information related to the group index n_g and its perturbation $\partial n_g/\partial \sigma$ which are given by:

$$n_g = n_{eff} - \lambda \left(\frac{\partial n_{eff}}{\partial \lambda} \right) \tag{4}$$

$$\frac{\partial n_g}{\partial \sigma} = \frac{\partial n_{eff}}{\partial \sigma} - \frac{\partial}{\partial \sigma}\left(\frac{\partial n_{eff}}{\partial \lambda}\right)\lambda \tag{5}$$

Combining Eq. 5 and Eq. 3 we can re-express the group index sensitivity in terms of the effective index sensitivity S_2:

$$S_3 \equiv \frac{\partial n_g}{\partial \sigma} = S_2 - \lambda \frac{\partial S_2}{\partial \lambda} \tag{6}$$

Therefore, the perturbation of group index is equal to that of the effective index $\partial n_{eff}/\partial \sigma = \partial n_g/\partial \sigma$ only if dispersion is constant throughout the experiment, i.e. $\frac{\partial}{\partial \sigma}(\partial n_{eff}/\partial \lambda)\lambda = 0$, or equivalently if the phase sensitivity, as defined in Eq. 3, is constant versus wavelength such that $\frac{\partial S_2}{\partial \lambda} = 0$. The observed outperformance of our 3-L sensor with respect to the starting model suggests that this contribution becomes non-negligible and suggests that S_2 is larger at shorter wavelengths. The introduction of isotropic or anisotropic thin cladding layers and modifications in the evanescent region of guided modes is known to play a key role in tailoring confinement and hence dispersion [32–34]. Here, our data suggests the 3-L sensor achieves a favorable sensitivity dispersion. Notably, this effect is not likely to appear in conventional evanescent sensors which would exhibit a decaying confinement factor in the active sensing region at shorter wavelengths and because modal dispersion is dominated by the arrangement of the bulk materials. In the 3-L device however, the core and top cladding material properties are changing significantly in response to surface adlayer attachment, $\Delta n \sim 0.05$, and with a differential sensitivity owing to the different mean porosity and pore sizes in each layer [29]. Assuming sensitivity dispersion as the dominant source of discrepancy between the starting model and experiment suggests that the 3-L waveguide dispersion is modified by as much as $\frac{\delta}{\delta \sigma}\left(\frac{dn_{eff}}{d\lambda}\right) \approx 1.56 \times 10^{-5} \frac{RIU}{nm} nm^{-1}$ at $\lambda = 1600$ nm. This observation suggests that device sensitivity may be further enhanced in the future by specifically engineering the effective medium design and waveguide dispersion. This highlights another unique capability of on-chip optics, and sub-wavelength engineered devices and metamaterials, which is not possible in conventional bulk Fabry-Perot interferometers.

3.4 Data Summary

The measured group index shifts from the sensing experiments are summarized in Table 1.

Table 1. Summary of measured changes in group index (Δn_g) from oxidation and silane attachment.

Waveguide Type	Width	Δn_g(ox)	Δn_g(silane)	Δn_g(ox)/n_g	Δn_g(sil)/n_g(ox)
2-L	900 nm	0.105	0.057	0.052	0.030
	500 nm	0.109	0.059	0.056	0.032
3-L	700 nm	0.249	0.082	0.127	0.048
	600 nm	0.252	0.078	0.126	0.044

Fig. 8 shows the modeled refractive index change and measured group index change respectively for both 2-L and 3-L waveguides compared side by side to modeled and measured effective index change of SOI waveguides to varying small molecule adlayer attachments.

More than 100x higher sensitivity is observed in both modeled and measured 2-L and 3-L waveguides compared to evanescent SOI sensors [3].

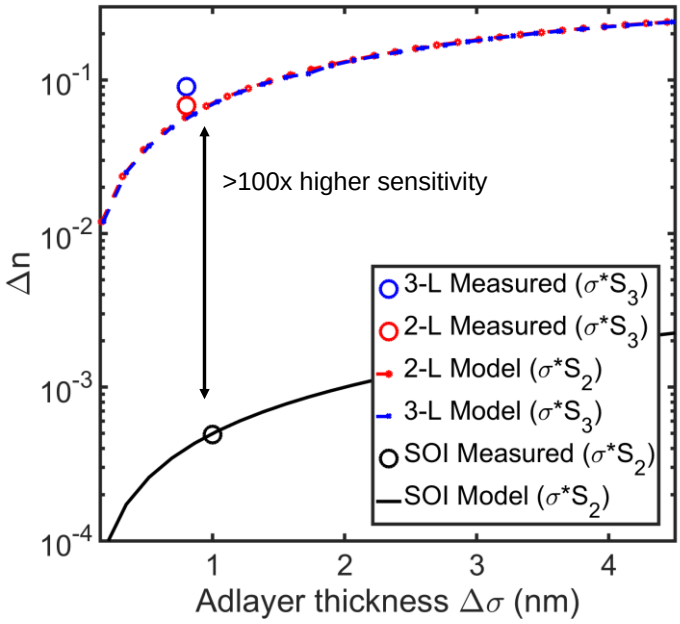

Fig. 8. Theoretical and experimental data of waveguide effective (group) index change σS_2 (S_3) vs. adlayer thickness of 2-L and 3-L pSi waveguides and optimized SOI waveguides from Ref. [3].

4. Conclusion

In summary, we demonstrate the design and fabrication of a unity confinement factor surface adlayer biosensor which displays a surface sensitivity two orders of magnitude greater than evanescent SOI waveguide sensors. Our design displays an attractive single mode characteristic where the sensitivity is consistent regardless of the spatial design parameters owing to the confinement factor being saturated near unity. We also demonstrated an inverse processing technique wherein bulk silicon is pre-patterned before anodization, as a simple and scalable route for realizing porous silicon photonics. Lastly, in our investigation of waveguide interferometers operating in the unity confinement factor regime, we identify dispersion as a promising new degree of freedom for achieving future sensitivity enhancements.

Appendix A: Experimental section

Patterning: 4-inch (100) p+ silicon wafers (0.01 Ω-cm) are first patterned using electron beam lithography (JEOL 9300FS 100kV) and reactive ion etching (C_4F_8 – 27 sccm, SF_6 – 12 sccm, Ar – 2 sccm) to fabricate silicon ribs with widths ranging from 0.3 to 2.5 microns at a dry etch depth of ~650 nm.

Porous Silicon Etching: Patterned Si wafers are diced into ~3 cm x ~3 cm dies and anodized in a 15% ethanoic hydrofluoric acid solution using a 55 mA/cm^2 current density for the lower index cladding ($n_{clad} \approx 1.56$) and 4.92 mA/cm^2 current density for the higher index core

($n_{core} \approx 2.1$). For the 2-layer design the anodization conditions are: 4.92 mA/cm^2 for 177 seconds and 55 mA/cm^2 for 70 seconds. This corresponds to thicknesses of approximately 800 nm for the core (layer 1) and 2050 nm for the cladding (layer 2). For the 3-L design the anodization conditions are: 55 mA/cm^2 for 4.5 seconds, 4.92 mA/cm^2 for 118 seconds, then 55 mA/cm^2 for 77 seconds. This corresponds to thicknesses of approximately 180nm, 650nm, and 2250 nm for the three layers. A Keithley DC current source is used for the etch systems. Etched waveguides are placed inside a 500°C furnace for 5 minutes for oxidation.

Numerical Modeling: Waveguide simulation is performed using a commercial eigenmode solver (Lumerical MODE Solutions). Porous silicon layers are modelled at a wavelength of 1600 nm using a Bruggeman effective medium approximation, assuming a pore diameter of ~15 nm for the core layer and ~35 nm for the cladding layer [29]. Refractive index profiles are modelled as isotropic. We note that a more rigorous approach would implement a spatially varying permittivity tensor to be implemented to account for the anisotropy and local rotation in the pore orientation.

Optical Measurements: We use a near-IR tunable laser (Santec TSL-510) with wavelength sweep capabilities from 1560-1680 nm with a photodetector (Newport 918D-IR-OD3R) coupled to a power meter (Newport 2936-R). Interchangeably, an infrared camera (Hamamatsu c2741) is used at the output facet for imaging (Fig. 4e, 4f). We also use a polarizer at the output facet to identify and tune into the TE or TM polarization modes using a manual polarization controller. The captured spectrum is analyzed by running a fast Fourier transform where the peak corresponds to the total path length $2n_gL$ where n_g is the group index and L is the length of the Fabry-Perot cavity [35].

Funding

National Science Foundation (NSF) Award 1825787 and EEC-1560070.

Acknowledgements

A portion of this research was conducted at the Center for Nanophase Materials Sciences, which is a DOE Office of Science User Facility. G.A. and J.R. which to acknowledge Dr. Rod Harrell for leading the Clemson Summer Undergraduate Research Experience (SURE) program in Solid-State Devices for Electronics, Photonics, and Magnetics Technology (NSF EEC-1560070).

References

1. X. H. Wang and S. Wang, "Sensors and biosensors for the determination of small molecule biological toxins," Sensors **8**, 6045–6054 (2008).
2. Y. Zhuo and B. T. Cunningham, "Label-free biosensor imaging on photonic crystal surfaces," Sensors (Switzerland) **15**, 21613–21635 (2015).
3. S. TalebiFard, S. Schmidt, W. Shi, W. Wu, N. A. F. Jaeger, E. Kwok, D. M. Ratner, and L. Chrostowski, "Optimized sensitivity of Silicon-on-Insulator (SOI) strip waveguide resonator sensor," Biomed. Opt. Express **8**, 500 (2017).
4. M. Iqbal, M. A. Gleeson, B. Spaugh, F. Tybor, W. G. Gunn, M. Hochberg, T. Baehr-Jones, R. C. Bailey, and L. C. Gunn, "Label-Free Biosensor Arrays Based on Silicon Ring Resonators and High-Speed Optical Scanning Instrumentation," IEEE J. Sel. Top. Quantum Electron. **16**, 654 (2010).
5. C. C. Evans, C. Liu, and J. Suntivich, "TiO2 nanophotonic sensors for efficient integrated evanescent-Raman spectroscopy," ACS Photonics acsphotonics.6b00314 (2016).
6. F. J. G. De Abajo, V. Pruneri, and H. Altug, "Mid-infrared plasmonic biosensing with graphene," Science **349**, 165–168 (2015).
7. T. Yoshie, L. Tang, and S. Y. Su, "Optical microcavity: sensing down to single molecules and atoms,"

Sensors **11**, 1972 (2011).
8. Y. Xu, P. Bai, X. Zhou, Y. Akimov, C. E. Png, L. Ang, W. Knoll, and L. Wu, "Optical Refractive Index Sensors with Plasmonic and Photonic Structures : Promising and Inconvenient Truth," Adv. Opt. Mater. **7**, 1–47 (2019).
9. G. Testa, G. Persichetti, and R. Bernini, "Liquid core ARROW waveguides: A promising photonic structure for integrated optofluidic microsensors," Micromachines **7**, (2016).
10. H. Li and X. Fan, "Characterization of sensing capability of optofluidic ring resonator biosensors," Appl. Phys. Lett. **97**, 3–6 (2010).
11. G. Rong, A. Najmaie, J. E. Sipe, and S. M. Weiss, "Nanoscale porous silicon waveguide for label-free DNA sensing," Biosens. Bioelectron. **23**, 1572–1576 (2008).
12. G. A. Rodriguez, S. Hu, and S. M. Weiss, "Porous silicon ring resonator for compact, high sensitivity biosensing applications," Opt. Express **23**, 7111 (2015).
13. R. Caroselli, S. Ponce-Alcántara, F. P. Quilez, D. M. Sánchez, L. T. Morán, A. G. Barres, L. Bellieres, H. Bandarenka, K. Girel, V. Bondarenko, and J. García-Rupérez, "Experimental study of the sensitivity of a porous silicon ring resonator sensor using continuous in-flow measurements," Opt. Express **25**, 31651–31659 (2017).
14. P. Azuelos, P. Girault, N. Lorrain, and Y. Dumeige, "Optimization of porous silicon waveguide design for micro-ring resonator sensing applications," J. Opt. **20**, 1–13 (2018).
15. G. I. A. R. Odriguez, P. E. T. R. M. Arkov, A. L. P. C. Artwright, M. O. H. C. Houdhury, F. R. O. A. Fzal, T. E. C. Ao, S. I. Ami, H. Alimi, S. C. T. R. Etterer, I. V. A. N. I. K. Ravchenko, and S. M. Haron, "Photonic crystal nanobeam biosensors based on porous silicon," Opt. Express **27**, 9536–9549 (2019).
16. J. D. Ryckman, M. Liscidini, J. E. Sipe, and S. M. Weiss, "Direct imprinting of porous substrates: A rapid and low-cost approach for patterning porous nanomaterials," Nano Lett. **11**, (2011).
17. D. J. Sirbuly, G. M. Lowman, B. Scott, G. D. Stucky, and S. K. Buratto, "Patterned microstructures of porous silicon by dry-removal soft lithography," Adv. Mater. **15**, 149–152 (2003).
18. B. P. Azeredo, Y. W. Lin, A. Avagyan, M. Sivaguru, K. Hsu, and P. Ferreira, "Direct Imprinting of Porous Silicon via Metal-Assisted Chemical Etching," Adv. Funct. Mater. 2929–2939 (2016).
19. J. T. Robinson, K. Preston, O. Painter, and M. Lipson, "First-principle derivation of gain in high-index-contrast waveguides," Opt. Express **16**, 16659–16669 (2008).
20. T. F. Krauss, "Slow light in photonic crystal waveguides," J. Phys. D. Appl. Phys. **40**, 2666–2670 (2007).
21. J. J. Ackert, J. K. Doylend, D. F. Logan, P. E. Jessop, R. Vafaei, and A. P. Knights, "Defect-mediated resonance shift of silicon-on- insulator racetrack resonators," Opt. Express **19**, 9431–9435 (2011).
22. T. Chung, S. Y. Lee, E. Y. Song, H. Chun, and B. Lee, "Plasmonic nanostructures for nano-scale bio-sensing," Sensors **11**, 10907–10929 (2011).
23. Y. Wan, N. A. Krueger, C. R. Ocier, P. Su, P. V Braun, and B. T. Cunningham, "Resonant Mode Engineering of Photonic Crystal Sensors Clad with Ultralow Refractive Index Porous Silicon Dioxide," Adv. Opt. Mater. **5**, 1–7 (2017).
24. F. Dell'Olio and V. M. N. Passaro, "Optical sensing by optimized silicon slot waveguides," Opt. Express **15**, 4977 (2007).
25. N. A. Krueger, A. L. Holsteen, S. K. Kang, C. R. Ocier, W. Zhou, G. Mensing, J. A. Rogers, M. L. Brongersma, and P. V. Braun, "Porous Silicon Gradient Refractive Index Micro-Optics," Nano Lett. **16**, 7402–7407 (2016).
26. J. Álvarez, P. Bettotti, I. Suárez, N. Kumar, D. Hill, L. Pavesi, and J. Martínez-pastor, "Birefringent porous silicon membranes for optical sensing," Opt. Express **19**, 26106–26116 (2011).
27. N. Ishikura, M. Fujii, K. Nishida, S. Hayashi, and J. Diener, "Dichroic rugate filters based on birefringent porous silicon Abstract :," Opt. Express **16**, 5091–5094 (2008).
28. G. Hermanson, *Bioconjugate Techniques* (Academic, 1996).
29. H. Ouyang, C. C. Striemer, and P. M. Fauchet, "Quantitative analysis of the sensitivity of porous silicon optical biosensors," Appl. Phys. Lett. **88**, 3–5 (2006).
30. N. Massad-ivanir, E. Segal, and S. Weiss, "Porous Silicon-Based Photonic Biosensors: Current Status and Emerging Applications," Anal. Chem. **91**, 441–467 (2019).
31. M. M. Orosco, C. Pacholski, and M. J. Sailor, "Real-time monitoring of enzyme activity in a mesoporous silicon double layer," Nat. Nanotechnol. **4**, 255–258 (2009).
32. H. A. L. Iang, Y. H. E. Ang, R. U. I. L. Uo, and Q. I. L. In, "Ultra-broadband dispersion engineering of nanophotonic waveguides," Opt. Express **24**, 13189–13194 (2016).
33. S. Jahani, S. Kim, J. Atkinson, J. C. Wirth, F. Kalhor, A. Al Noman, W. D. Newman, P. Shekhar, K. Han, V. Van, R. G. Decorby, L. Chrostowski, M. Qi, and Z. Jacob, "Controlling evanescent waves using silicon photonic all-dielectric metamaterials for dense integration," Nat. Commun. **9**, 1–9 (2018).
34. S. Jahani and Z. Jacob, "Transparent subdiffraction optics : nanoscale light confinement without metal," Optica **1**, 96–100 (2014).
35. C. Pacholski, M. Sartor, M. J. Sailor, F. Cunin, and G. M. Miskelly, "Biosensing using porous silicon double-layer interferometers: Reflective interferometric fourier transform spectroscopy," J. Am. Chem. Soc. **127**, 11636–11645 (2005).